



WO_x domain size, acid properties and mechanistic aspects of glycerol hydrogenolysis over Pt/WO_x/ZrO₂

Wei Zhou^a, Juan Luo^b, Yue Wang^a, Jianfeng Liu^{a,b}, Yujun Zhao^a, Shengping Wang^a, Xinbin Ma^{a,*}

^a Key Laboratory for Green Chemical Technology of Ministry of Education, Collaborative Innovation Centre of Chemical Science and Engineering, School of Chemical Engineering and Technology, Tianjin University, Tianjin 300072, China

^b Sinopec Shanghai Research Institute of Petrochemical Technology, Shanghai 201208, China



ARTICLE INFO

Keywords:
WO_x domain
Brønsted acid
Surface species
Glycerol
1,3-Propanediol

ABSTRACT

Supported WO_x catalysts are widely investigated in glycerol hydrogenolysis for their high selectivity to 1,3-propanediol (1,3-PDO). The high performance is often related to surface Brønsted acid site. However, the intrinsic structure of Brønsted acid is unclear and its controllable preparation has not been investigated in detail. In addition, many reaction mechanisms have been proposed up to now, but with few direct evidences in spectroscopy studies. In this work, Pt/WO_x/ZrO₂ catalysts containing various amounts of WO_x were studied in glycerol hydrogenolysis. The reaction is found to be structurally sensitive to WO_x domain size, with medium polymerized WO_x shown to benefit the formation of 1,3-PDO. By doping a suitable amount of Mn into monolayer covered WO_x/ZrO₂, large amounts of WO_x with medium polymerization degree were created. Thus, the turnover frequency of 1,3-PDO (TOF_{1,3-PDO/W}) increased 2.6 times in comparison to the best result of none Mn-doping Pt/WO_x/ZrO₂ catalysts. Characterizations of WO_x structure and acid properties indicate that super strong Brønsted acid site is created by the interaction between medium polymerized WO_x and Pt particle. This type of acid is linearly correlated with the formation rate of 1,3-PDO. The adsorption state of glycerol was studied using infrared spectroscopy, and the secondary –OH is found to be strongly adsorbed to Brønsted acid site on WO_x containing catalyst, while its interaction with Pt/ZrO₂ is much weaker. The natural structure of the active site is proposed to be Pt-(WO_x)_n-H, integrating super strong Brønsted acid site and metallic Pt site together. Combined with FTIR investigations of different surface hydrogen species and in situ 2-propanol conversion, the reaction mechanism was also determined.

1. Introduction

The conversion of biomass to energy and chemicals can alleviate the pressure of fossil energy exhaustion, and also benefits the reduction of CO₂ emission because of its carbon neutral property [1]. Glycerol is one of the most important building blocks of biomass, and with the fast development of biodiesel production, its transformation becomes a hot topic in green chemistry [2–5]. One of the routes is the hydrogenolysis of glycerol to propanediols (PDOs), which can be used as monomers in polyester industry.

Because of the high selectivity for dehydration and hydrogenation of C–O structure, Cu based catalysts are widely used in glycerol hydrogenolysis to 1,2-PDO, and catalysts with 1,2-PDO yield higher than 90% have been reported by many groups [1]. However, the production of 1,3-PDO from glycerol hydrogenolysis remains a challenge. Firstly, the secondary hydroxyl group is steric hindered by two primary

hydroxyls, making it less accessible to the active sites of catalysts. Secondly, for the two types hydroxyl groups, their dehydration activation energies based on neutral glycerol are similar (70.9 kcal mol^{−1} for 2° –OH and 73.2 kcal mol^{−1} for 1° –OH), and their proton affinities are nearly the same (195.4 kcal mol^{−1} for 2° –OH and 194.8 kcal mol^{−1} for 1° –OH) [6]. Such small differences on reactivity make it very difficult to improve 1,3-PDO selectivity. In addition, because high temperatures can lead to deep hydrogenolysis of PDOs, the reaction should be carried out in mild conditions, generally below 200 °C [7]. Therefore, to achieve a better activity, strong acid especially Brønsted acid site should be the essential component of catalyst. Up to now, bifunctional catalysts are the main materials used in glycerol hydrogenolysis to 1,3-PDO, with metal sites to activate H₂ and acid sites to activate glycerol. Among them, ReO_x and WO_x based catalysts are widely studied, and the importance of Brønsted acid for 1,3-PDO formation has been emphasized for both catalysts [8–17].

* Corresponding author.

E-mail address: xbma@tju.edu.cn (X. Ma).

Among WO_x based catalysts, WO_x/ZrO_2 is categorized as a solid super acid, which was first reported by Hino and Arata in 1988 [18]. Due to their strong acidity and great hydrothermal stability, WO_x/ZrO_2 and $\text{Pt}/\text{WO}_x/\text{ZrO}_2$ have been widely applied in catalytic reactions such as isomerization [19,20], NO_x reduction [21,22], alcohol dehydration [23], esterification [24,25], as well as glycerol hydrogenolysis [10,26]. A suitable WO_x loading is necessary for the good performance, and volcano curves between activity and WO_x surface density or polymerization are usually found in these reactions. Higher WO_x loading above monolayer coverage results in the formation of bulk WO_3 and decrease of the number of acid sites. So some methods have been proposed to improve the specific surface area or monolayer threshold of the materials [27,28]. The nature of the active acid site of WO_x/ZrO_2 has also been discussed for a long time. Recently, Zhou et al. overviewed previous perspectives and their comprehensive studies with the help of in situ UV-vis DRS, Raman and STEM-HAADF characterization, as well as theoretical calculations. They confirmed that three-dimensional distorted $\text{Zr}-\text{WO}_x$ clusters (0.8–1.0 nm) are the most active catalytic species due to the strongest Brønsted acid [29]. It is worth discussing whether this model is also applicable for bifunctional $\text{Pt}/\text{WO}_x/\text{ZrO}_2$ catalysts in glycerol hydrogenolysis.

The reaction mechanisms of 1,3-PDO formation over $\text{Pt}-\text{WO}_x$ catalysts are widely discussed and two routes are mainly proposed. One is dehydration-hydrogenation route, in which glycerol is firstly dehydrated to 3-hydroxy propionaldehyde (3-HPA), then the intermediate is converted to 1,3-PDO via hydrogenation [16,30,31]. The second route involves the formation of secondary carbocation intermediate (by direct dehydroxylation of $2^\circ - \text{OH}$) and follows by the attack of activated hydrogen species [12,13,15,32]. However, most mechanisms were based on product distributions over different catalysts and reaction conditions. The adsorption state of glycerol on catalyst surface and the confirmation of intermediates (3-HPA or secondary carbocation) are rarely reported. Another important issue is surface hydrogen species. It was mentioned by many groups that H_2 pressure has significant effects in glycerol hydrogenolysis [10,12,13,33], while different surface hydrogen species have also been proposed in reaction mechanisms [10,14,33,34]. Furthermore, there are various kinds of hydrogen species on the surface of $\text{Pt}/\text{WO}_x/\text{ZrO}_2$, and five situations are summarized here in Fig. 1: (1) Dissociative adsorbed H species on Pt metal site, (2) permanent Brønsted acid on WO_x species, (3) temporary Brønsted acid formed by the reduction of WO_x species [35,36], (4) proton and hydride pairs formed by H_2 heterolysis on WO_x species [10,12], (5) hydride captured by the ZrO_2 support [37]. Direct evidence is still needed to understand which situation contributes to the formation of 1,3-PDO.

In this work, the domain size of surface WO_x under monolayer coverage was controlled by two methods: (1) increasing the polymerization degree by changing WO_x loading, (2) decreasing the polymerization degree by Mn doping into WO_x/ZrO_2 with monolayer coverage. And its effect on 1,3-PDO formation was investigated in glycerol hydrogenolysis. The structures and acid properties were comprehensively characterized and the natural active site was proposed. FTIR studies provided evidences on the adsorption state of glycerol and surface hydrogen species that participated in the reaction. Combined with in situ study of 2-propanol conversion, the reaction mechanism was also given.

2. Experimental

2.1. Catalyst synthesis

Tetragonal ZrO_2 precursor was prepared by the solvothermal method [38]. Zirconyl nitrate ($\text{ZrO}(\text{NO}_3)_2 \cdot 2\text{H}_2\text{O}$, > 45.0% ZrO_2 , Tianjin Guangfu Fine Chemical Research Institute) and urea ($\text{CO}(\text{NH}_2)_2$, > 99.0%, Tianjin Kemiou Chemical Reagent Co., Ltd) were dissolved in 50 mL methanol (CH_3OH , > 99.0%, Tianjin Kemiou Chemical Reagent Co., Ltd), with the Zr^{4+} concentration of 0.4 M and Zr^{4+} /urea mole ratio of 1/10. Then the solution was transferred to a 100 mL stainless-steel autoclave with a Teflon liner and kept at 140 °C for 12 h. The obtained deposition was filtered and dried at 100 °C overnight. WO_x/ZrO_2 samples were prepared by the incipient wetness impregnation method. ZrO_2 precursor was impregnated with various amounts of ammonium metatungstate ($(\text{NH}_4)_6(\text{H}_2\text{W}_{12}\text{O}_{40}) \cdot n\text{H}_2\text{O}$, > 99.9%, J&K Chemical Corp.) dissolved in deionized water. After dried at 100 °C overnight, it was calcined at 700 °C for 4 h with a heating rate of 2 °C/min. For the preparation of Mn containing samples, Mn element was introduced by co-impregnation with ammonium metatungstate, and manganese acetate ($\text{Mn}(\text{CH}_3\text{COO})_2 \cdot 4\text{H}_2\text{O}$, > 99.9%, Real&Lead Co., Ltd) was used as precursor.

Pt was impregnated on the oxide supports using an aqueous solution of chloroplatinic acid ($\text{H}_2\text{PtCl}_6 \cdot 6\text{H}_2\text{O}$, > 37.0% Pt, Real&Lead Co., Ltd.), with a final Pt loading of 2 wt %. After dried at room temperature, the sample was calcined at 350 °C for 2 h. The powder was reduced at 250 °C for 2 h before reaction. The obtained catalysts were labelled as Pt/ZrW_x and $\text{Pt}/\text{ZrW}_{38}\text{Mn}_x$, where x presents the loading of WO_x species or Mn element (wt %), respectively. The WO_x loading was fixed to 38 wt % for Mn containing samples.

2.2. Catalyst characterization

X-ray powder diffraction (XRD) patterns of the catalysts were recorded using a Rigaku D/MAX-2500 diffractometer with a $\text{Cu K}\alpha$ radiation source ($\lambda = 1.5406 \text{ \AA}$). The scanning angle (2θ) ranged from 20° to 90°, with a speed of 10°/min. Scherrer equation was used to calculate the mean crystallite size of particles.

Nitrogen adsorption was carried out on an ASAP 2020 instrument at –196 °C. Samples were degassed at 300 °C under N_2 flow for 3 h before measurement. The surface area of sample was calculated by BET method, and the W surface density, ρ_W (the number of W atoms located on ZrO_2 surface, W atoms/ nm^2), was estimated from the corrected surface area of ZrO_2 [39,40].

Raman spectra were determined at room temperature in atmosphere on a LabRAM ARAMIS Raman spectrometer (HORIBA Scientific), with a visible excitation of 532 nm. System alignment was verified with a silica reference standard before the sample scanning. The final spectrum was obtained after 15 scans accumulated, with a speed of 20 s/scan.

Ultraviolet-visible diffuse reflectance spectra (UV-vis DRS) were obtained from a Shimadzu UV-2550 spectrophotometer in the range of 200–800 nm, with BaSO_4 as the background. The sample was grounded to fine powder and dried at 100 °C overnight before spectra collection. The Kubelka-Munk $F(R_\infty)$ function was calculated from the absorbance of the UV-vis DRS, and the edge energy (E_g) for indirect transitions [41] was given by the intercept of the straight line in the low-energy rise of a plot of $[F(R_\infty)h\nu]^{0.5}$ versus $h\nu$, where $h\nu$ denotes the incident photon energy.

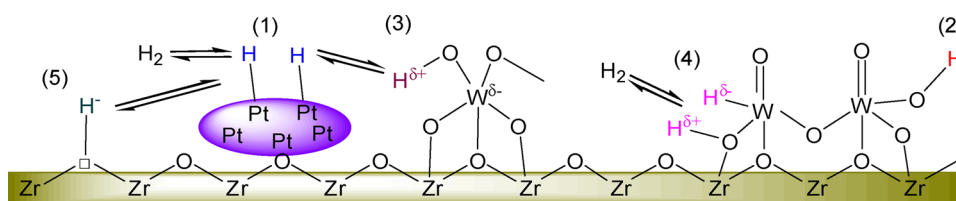


Fig. 1. Various types of hydrogen species on $\text{Pt}/\text{WO}_x/\text{ZrO}_2$ surface.

To estimate the dispersion of Pt particles, CO chemisorption was carried out in a microreactor system equipped with a Cirrus 200 mass spectrometer (MKS). About 50 mg (40–60 mesh) of catalyst was first reduced under H_2 for 2 h at 250 °C, and then purged by He for another 30 min. After cooling to room temperature, pulses of 5% CO/He were introduced until the CO peak area was stable. The mole ratio of adsorbed CO/Pt was defined as 1.0.

H_2 chemisorption and H_2 -temperature programmed reduction (TPR) were conducted on a Micromeritics Autochem II 2920 chemisorption analyzer equipped with a thermal conductivity detector (TCD). In H_2 chemisorption, about 100 mg of sample was put into a U-shaped quartz tube and reduced at 250 °C for 2 h in 10% H_2 /Ar. After purging with Ar for 30 min at 300 °C, the temperature was decreased to 50 °C and then 10% H_2 /Ar pulse injection was performed until the TCD peaks became stable. H/Pt value is defined as the moles of adsorbed H atoms per mole of surface Pt on the catalyst. For TPR, the sample was pre-treated at 300 °C for 1 h under Ar. After cooling to 50 °C, TPR using 10% H_2 /Ar was started with a heating rate of 10 °C/min.

NH_3 temperature-programmed desorption (TPD) was also measured on the same instrument. After pretreated in He flow at 300 °C for 1 h, the sample was cooled to 50 °C and exposed to 10% NH_3 /He flow for 30 min. Then it was purged in He until the baseline was stable, and the TPD program started to run from 50 °C to 600 °C with a ramping rate of 10 °C/min. For Pt containing catalysts, the reduction under 10% H_2 /Ar was performed before He pretreatment.

All of the Fourier transform infrared (FTIR) spectra experiments were performed on a Nicolet 6700 spectrometer equipped with a heating cell, a MCT/A detector, as well as a gas/vacuum system. About 30 mg of the sample was pressed to a wafer at 5 MPa and weighed again before the measurement.

FTIR spectra of pyridine adsorption were applied to characterize the acid properties of supports. The sample was put into a heating cell, and then pretreated at 350 °C for 1 h under vacuum of 10^{-4} Pa. After cooling to 180 °C, the background was scanned and 0.4 μ L of pyridine was introduced into the closed system and kept for 30 min. After the adsorption, the physically adsorbed pyridine was desorbed under vacuum for another 30 min, and the result was collected. Areas of the characteristic peaks at 1538 and 1446 cm^{-1} were integrated to give quantitative analysis of Brønsted and Lewis acid sites. The extinction coefficients were calculated based on the work of Emeis [42].

Under H_2 atmosphere, the adsorbed pyridine can be reduced to piperidine even at 30 °C, which would cause interference to the quantitative analysis. To investigate the effect of Pt metal and H_2 species on the acid properties, FTIR spectra of NH_3 adsorption under H_2 atmosphere were studied instead of pyridine, combined with TPD process. After sample was reduced at 250 °C, NH_3 adsorption was carried out in 10% H_2 /Ar flow for 15 min. Then, the system was purged in He flow, and NH_3 -TPD spectra were recorded from 250 °C to 450 °C, with a ramp rate of 10 °C/min. For comparison, the adsorption was also conducted under O_2 flow.

Adsorbed H_2 species on the surface of catalysts were characterized by in situ FTIR spectra. The sample was reduced at 250 °C for 2 h under 10% H_2 /Ar and purged in He at 450 °C for 30 min. The background was collected after cooling to 180 °C, and then 10% H_2 /Ar was introduced to the system for 1 h and H_2 adsorption spectrum was recorded.

In situ reaction of 2-propanol (PO) and H_2 over catalysts was also investigated by FTIR spectra. After reduction, the background of catalyst was scanned at 180 °C under the H_2 atmosphere. Then, 0.4 μ L 2-PO was injected to the system and the spectrum was recorded continuously until it was stable. Results with the highest intensity of adsorbed substrates were analyzed.

The FTIR spectra of glycerol adsorption with low coverage on supports and catalysts were also studied. The sample wafer was moistened by drops of distilled water and stabilized at room temperature under He flow. After the background was collected, 0.2 μ L glycerol aqueous solution with a concentration of 1.0 wt % was dropped onto the sample.

The result was obtained after the spectrum was stable in flowing He. For the investigation at different temperature, the sample was not moistened before glycerol adsorption.

DRIFT spectra of CO adsorption on catalysts were also obtained on the same instrument. The powder sample was put into a diffuse reflection cell. After reduction and purging with He, sample was cooled to 30 °C, and the background was scanned. Subsequently, CO was introduced and the adsorption was continued for 30 min. Then the sample was purged again and the spectrum was obtained after the peaks were stable.

2.3. Catalytic reactions

0.5 g catalyst was reduced at 250 °C for 2 h and transferred into 40 g glycerol aqueous solution (10 wt %) in a stainless steel autoclave of 100 mL. After purging with H_2 for several times, the pressure of the system was increased to 5.5 MPa. The reaction was performed at 180 °C, 8 MPa for 18 h, with the stirring rate of 1000 rpm. After cooling to room temperature, the liquid products were analyzed using a gas chromatograph (Agilent Micro GC 4890) with a flame ionization detector and a DB-FFAP capillary column (Agilent, 30 m × 0.32 mm × 1.00 μ m). *n*-Butanol and 1,4-butanediol were used as the internal standards. The gas phase was collected by a gas bag and analyzed by an Agilent GC 7890B gas chromatograph equipped with a flame ionization detector and a HP-AL/S column (Agilent, 25 m × 0.32 mm × 8.00 μ m). Generally, the carbon mass balance was found to be > 98% in liquid phase and little amounts of propane, ethane and methane were found in the gas products. The conversion of glycerol and the selectivity of each product are defined as follows:

$$\text{conversion (\%)} = (\text{moles of converted glycerol}) / (\text{moles of inlet glycerol})$$

$$\text{selectivity (\%)} = (\text{moles of glycerol required for specific product}) / (\text{moles of converted glycerol})$$

3. Results and discussion

3.1. WO_x domain size adjustment and catalytic promotion strategy

3.1.1. Structural properties and catalytic performance of $Pt/ZrWx$

Fig. 2a shows the crystalline structures of $Pt/ZrWx$ samples. Monoclinic ZrO_2 is mainly presented on Pt/ZrO_2 , as it is thermodynamically stable during high temperature calcination. With the increase of WO_x loading, the intensity of monoclinic ZrO_2 decreases and tetragonal ZrO_2 becomes to the only phase, demonstrating that WO_x stabilizes the tetragonal phase and suppresses the formation of monoclinic ZrO_2 [43]. There are no diffraction peaks of Pt and WO_3 for all samples, indicating their high dispersion on ZrO_2 support. However, when the WO_x loading is increased to 42%, bulk WO_3 emerges on the catalyst (Fig. S1). Therefore, the monolayer coverage of WO_x on ZrO_2 is reached at WO_x loading of about 38%, which is consistent with the result of Song et al. [27].

To further illustrate the state of surface WO_x , Raman and UV-vis DRS of the supports are given in Fig. 2b and c, respectively. Raman bands of ZrO_2 are typically in the frequency range below 700 cm^{-1} , and Fig. 2b shows that t- ZrO_2 is mainly presented in these WO_x containing samples, with its characteristic bands at 148, 271, 314, 461, and 644 cm^{-1} [44]. Weak intensity of m- ZrO_2 phase (Raman bands at about 178, 189, and 381 cm^{-1}) is also found in $ZrW5$, which is consistent with XRD. For WO_x structure, the Raman band at about 834 cm^{-1} is assigned to W–O or W–O–W stretching modes [45], and 960–990 cm^{-1} region is related to the vibrations of hydrated W=O mode [45–48]. With the increase of WO_x species, the Raman band of W–O–W mode shifts from 834 to 811 cm^{-1} , and the band of hydrated W=O mode also shifts from 964 to 988 cm^{-1} , which reflects a gradual

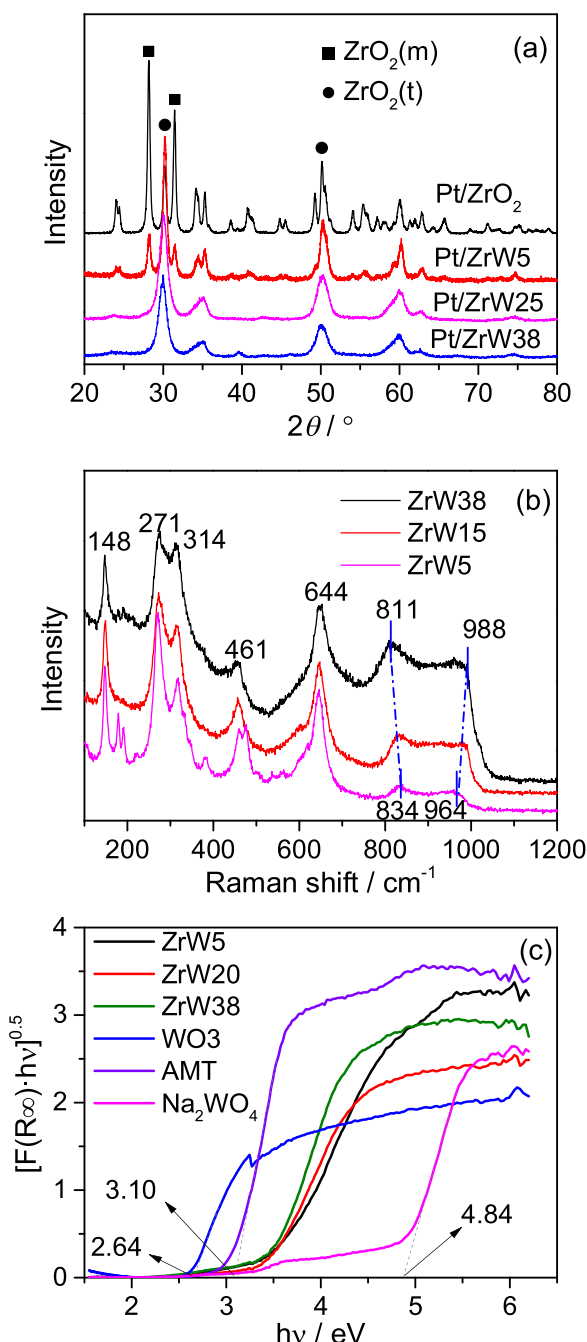


Fig. 2. Structure characterization of WO_x domains on ZrW_x based samples. (a) XRD patterns of Pt/ZrW_x catalysts. (b) Raman spectra of ZrW_x supports. (c) UV-vis DRS of ZrW_x supports. AMT: ammonium metatungstate.

polymerization of WO_x [45,46]. In addition, bands of bulk WO_3 (805 and 715 cm^{-1}) are not found in the Raman spectrum of ZrW₃₈, combined with XRD results, indicating that WO_x on ZrW₃₈ is almost at the monolayer coverage.

The polymerization degree of WO_x species on ZrO_2 can also be characterized by the edge energy derived from UV-vis DRS [41,46]. For comparison, results of standard compounds (WO_3 , ammonium metatungstate and Na_2WO_4) with different WO_x polymerization are also given. As shown in Fig. 2c, Na_2WO_4 containing isolated WO_4 species has the highest E_g value (4.84 eV), and WO_3 with 3D network structure gives the lowest E_g (2.64 eV). Ammonium metatungstate with W_{12} clusters has an intermediate E_g of 3.10 eV. The edge energies of three standard compounds are coincident with the results of Barton et al. [41]

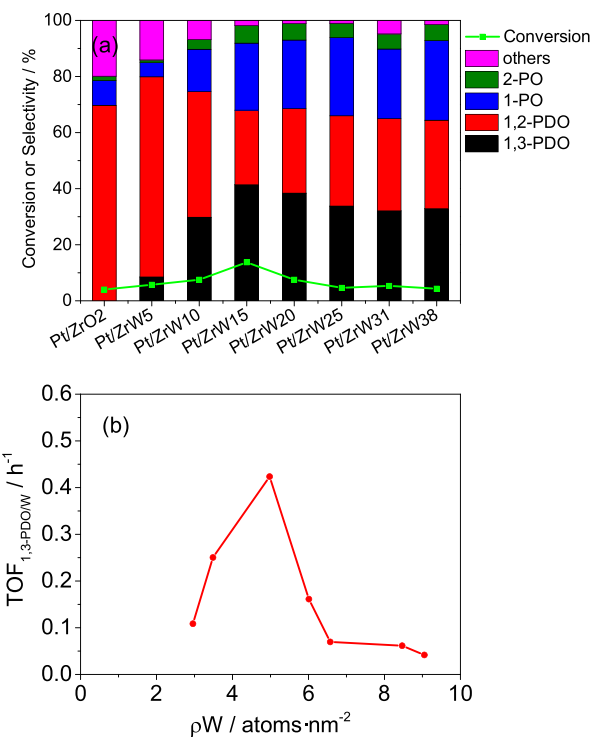


Fig. 3. Performances of Pt/ZrW_x catalysts in glycerol hydrogenolysis. (a) Glycerol conversion and product selectivity. (b) The correlation between $\text{TOF}_{1,3\text{-PDO}/W}$ and W surface density. Reaction conditions: 4.0 g glycerol, 36.0 g water, 0.5 g catalyst, 180 °C, 8 MPa, 1000 rpm, 18 h. 1,3-PDO: 1,3-propanediol; 1,2-PDO: 1,2-propanediol; 1-PO: 1-propanol; 2-PO: 2-propanol; others include ethylene glycol, ethanol, and methanol.

The polymerization degree of ZrW_x samples are all between Na_2WO_4 and ammonium metatungstate, and the absorption spectra shift to lower energies with the increase of WO_x loading, indicating a gradual polymerization of surface WO_x units, consistent with Raman spectra.

The performances of Pt/ZrW_x in glycerol hydrogenolysis at 180 °C are shown in Fig. 3a. A volcano curve is presented for the correlation between glycerol conversion and WO_x loading, with the highest conversion (13.7%) and 1,3-PDO selectivity (41.4%) obtained on Pt/ZrW₁₅. With the increase of WO_x loading, the selectivity of 1,3-PDO sharply increases from 0.0% to 41.4%, and then drops slowly to 32.0%. This indicates a medium amount of WO_x is suitable to the reaction. To further illustrate it, surface density of W element (ρW , atoms $\cdot \text{nm}^{-2}$) was calculated (Table S1) and its correlation with 1,3-PDO formation rate per WO_x site ($\text{TOF}_{1,3\text{-PDO}/W}$, h⁻¹) is given in Fig. 3b. Clearly, the reaction is structurally sensitive on WO_x domains. At W surface density of 5.0 atoms $\cdot \text{nm}^{-2}$, the WO_x domain is medium polymerized and shows the highest $\text{TOF}_{1,3\text{-PDO}/W}$ value.

3.1.2. Catalytic promotion strategy by Mn doping

As described above, more WO_x with medium polymerization degree would contribute to a more active catalyst, while the isolated WO_x or highly polymerized WO_x are not such efficient. However, increasing WO_x loading by the simple impregnation method may result in the co-existence of WO_x with various domain sizes, especially at sub-monolayer coverage. WO_x unit can migrate between these domains on ZrO_2 surface and be close to thermodynamic equilibrium at such high calcination temperature (700 °C). In this part, the size of WO_x domain is controlled in an innovative way, which is presented in Scheme 1. When introducing Mn element into monolayer covered ZrW₃₈, the highly polymerized WO_x will be depolymerized by the formation of more stable MnWO_4 nanoparticles during calcination. Moreover, the migration of WO_x can be hindered by these MnWO_4 nanoparticles. Therefore,

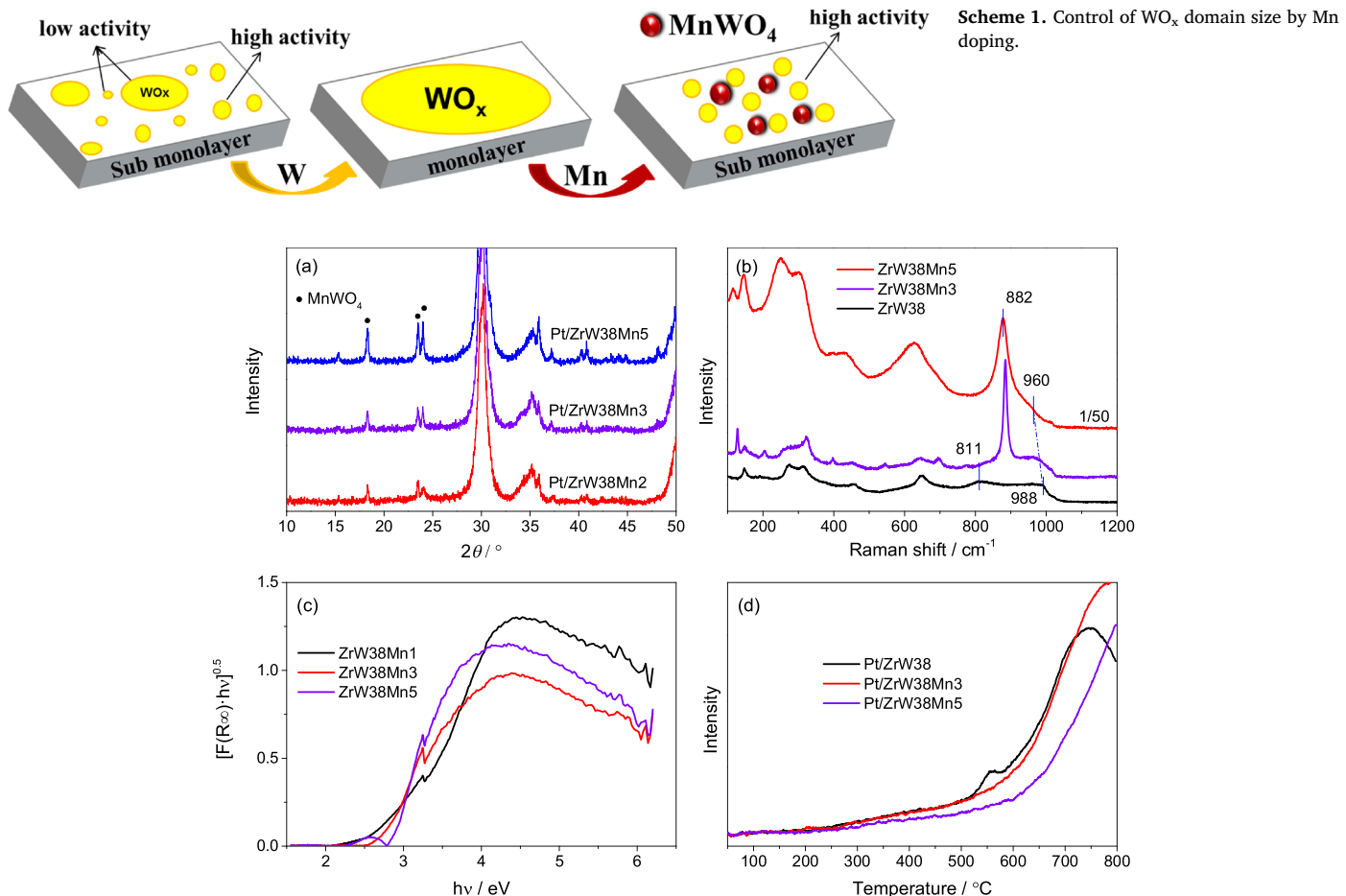


Fig. 4. Structure characterization of WO_x domains on Mn doped samples. (a) XRD patterns of Pt/ZrW38Mnx catalysts. (b) Raman spectra of ZrW38Mnx supports. (c) UV-vis DRS of ZrW38Mnx supports. (d) TPR profiles of Pt/ZrW38Mnx catalysts.

it is predicted that more WO_x domains with medium polymerized size can be obtained with a suitable amount of Mn.

As shown in Fig. 4a, the diffraction peaks of MnWO_4 appear and their intensities are enhanced with Mn content increasing, indicating a consumption of surface WO_x by the formation of MnWO_4 nanoparticles. This is accompanied with the change of WO_x domain size as evidenced by Raman spectra in Fig. 4b. With the addition of Mn, a strong characteristic band of MnWO_4 appears at 882 cm^{-1} [49], and W–O–W modes at 811 cm^{-1} is weakened. Notably, the band of hydrated W=O mode at 988 cm^{-1} shifts to 960 cm^{-1} . In addition, UV-vis DRS of Mn doped samples in Fig. 4c show the absorption spectra shift to higher energies with the increase of Mn loading. All of these demonstrate that Mn doping decreases the polymerization degree of WO_x . TPR can also reflect different WO_x domain size of the catalysts, as isolated WO_x species are harder to reduce than interconnected ones [19,47]. For Pt/ZrW samples, the reduction of WO_x species mainly contains three steps: $\text{WO}_3 \rightarrow \text{WO}_{2.9} \rightarrow \text{WO}_2 \rightarrow \text{W}$. The first reduction step gives a weak signal between 300 and 500 $^\circ\text{C}$, and then strong intensity of H_2 consumption is observed from 500 to 1200 $^\circ\text{C}$ [19]. Similar results are also obtained in this work, while the reduction signal higher than 800 $^\circ\text{C}$ is not measured because of the limitation of experimental condition. As shown in Fig. 4d, the reduction curve of Pt/ZrW38 is gradually raised with the increasing temperature and shows a weak peak at about 550 $^\circ\text{C}$, which is assigned to the first reduction step of WO_x domain. Then, a strong reduction peak is emerged at 750 $^\circ\text{C}$, indicating the second reduction step of WO_x . With the increase of Mn loading, the reduction of WO_x domain becomes difficult, as the weak peak for the first reduction step is not shown and the region of deeper reduction shifts to higher temperature. This indicates that the WO_x domain size is decreased after the

introduction of Mn, consistent with the results of Raman and UV-vis DRS. TPR profiles of Pt/ZrWx are also shown in Fig. S2. Although the deeper reduction peak moves to higher temperature on Pt/ZrW15, the peak of the first reduction step is still observed. Compared with Pt/ZrWMnx, this indicates that some of the highly polymeric WO_x domains are also existed on Pt/ZrW15, consistent with the model presented in Scheme 1. The reduction peak of Pt species was not observed here, as it was reduced under H_2 at 50 $^\circ\text{C}$ before TPR process.

The catalytic performances of Pt/ZrW38Mnx are given in Fig. 5a. Similar with Pt/ZrWx (Fig. 3a), a volcano trend is also obtained for Pt/ZrW38Mnx catalysts, but with a much higher conversion on Pt/ZrW38Mn3 (56.2%) than that on Pt/ZrW15 (13.7%). The selectivity of 1,3-PDO gradually increases from 32.1% to 50.6% during the addition of Mn element to 4%. After that, a significant drop (from 50.6% to 21.5%) occurs when Mn content reaches 5%. The trend of 1,3-PDO selectivity on the WO_x domain size is consistent with that in Fig. 3a, which suggests that excess WO_x species don't contribute to higher 1,3-PDO selectivity. The formation rate of 1,3-PDO on Pt/ZrW38Mn3 is among the top three results reported up to now, shown in Table S2.

The existence of bulk MnWO_4 contributes to surface area and causes inaccuracy to ρW calculation, so ρW of ZrW38Mnx is calculated by simplification (Table S3) and its correlation with $\text{TOF}_{1,3\text{-PDO/W}}$ is shown in Fig. 5b. As expected, by doping a suitable amount of Mn into ZrW38, medium polymerized WO_x domains, which are more active than other WO_x species, are increased and thus the $\text{TOF}_{1,3\text{-PDO/W}}$ is obviously enhanced. The highest $\text{TOF}_{1,3\text{-PDO/W}}$ is 1.09 h^{-1} (corresponding $\rho\text{W} = 3.5 \text{ atoms} \cdot \text{nm}^{-2}$) over Pt/ZrW38Mnx catalysts, which is about 2.6 times that of Pt/ZrWx (0.42 h^{-1}). In addition, the $\text{TOF}_{1,3\text{-PDO/W}}$ of Pt/ZrW38Mnx remains at a high value when ρW increases from 3.5 to 4.9

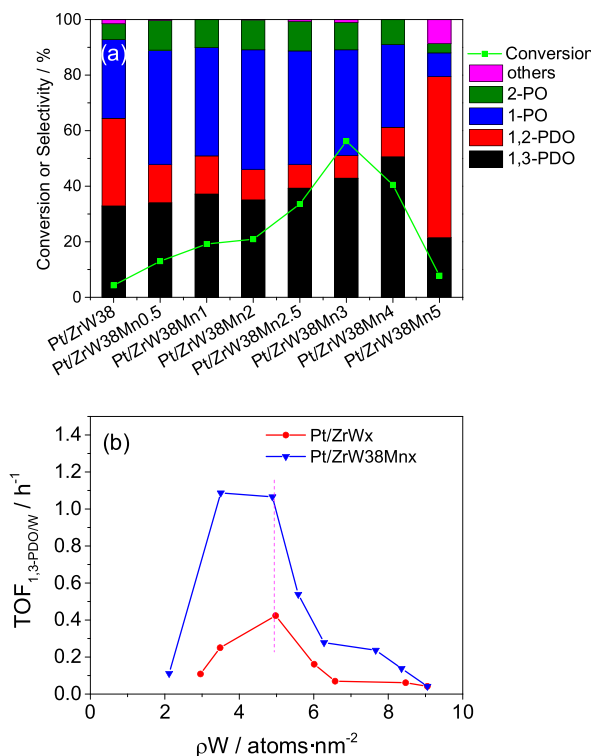


Fig. 5. Performances of Pt/ZrW38Mnx catalysts in glycerol hydrogenolysis. (a) Glycerol conversion and product selectivity. (b) The correlation between $\text{TOF}_{1,3\text{-PDO}/W}$ and W surface density. Reaction conditions are the same as those in Fig. 3.

atoms $\cdot \text{nm}^{-2}$, indicating that Mn doping allows WO_x domains to keep at a medium polymeric state with a wide range of W surface density.

For WO_x based catalysts in glycerol hydrogenolysis, supported Pt- WO_x materials are mostly reported because of their simple preparation method. Highly dispersed WO_x domains can be easily obtained by impregnation due to the strong interaction between WO_x and oxide supports such as Al_2O_3 and ZrO_2 . As the interaction is much weaker on SiO_2 support, mesoporous silica materials with large surface area are also used to achieve adequate active sites [15,31]. As shown in Table S2, the space time yield based on Pt metal (STY_{Pt}) of 1,3-PDO over these catalysts is often below $1.76 \text{ g}_{1,3\text{-PDO}} \cdot \text{g}_{\text{Pt}}^{-1} \cdot \text{h}^{-1}$. To achieve a higher activity, Zhang et al. developed mesoporous WO_x materials with the best STY_{Pt} of $3.98 \text{ g}_{1,3\text{-PDO}} \cdot \text{g}_{\text{Pt}}^{-1} \cdot \text{h}^{-1}$. But as reported in their work, the catalyst was sensitive to the preparation process [14]. There are two remarkable works among supported Pt- WO_x materials. One was reported by Arundhathi et al., with a STY_{Pt} value of $2.38 \text{ g}_{1,3\text{-PDO}} \cdot \text{g}_{\text{Pt}}^{-1} \cdot \text{h}^{-1}$ over Pt/ WO_x /AlOOH catalyst [50]. The other is from the work of Fan et al., using Pt- WO_x /t- ZrO_2 as catalyst and obtaining a STY_{Pt} of $5.26 \text{ g}_{1,3\text{-PDO}} \cdot \text{g}_{\text{Pt}}^{-1} \cdot \text{h}^{-1}$, which is the best result among the available literatures [17]. However, the structure–activity relationship is not fully elucidated in their work, and the intrinsic structure of active site is still ambiguous.

In our study, the reaction is found to be structurally sensitive on WO_x domain size. The control of WO_x domain size to a medium polymeric state will benefit the formation of 1,3-PDO. This is a principle for the rational synthesis of active site. From the standpoint of material synthesis, increasing WO_x loading is a kind of bottom-up method, which is difficult to achieve the size control of WO_x species by simple impregnation. On the contrary, the strategy of Mn doping proposed in Scheme 1 is a top-down method, which can create large amounts of WO_x domains with medium size. Thus, the best catalytic performance can be obtained on PtZrW38Mn3, giving a STY_{Pt} value of $4.43 \text{ g}_{1,3\text{-PDO}} \cdot \text{g}_{\text{Pt}}^{-1} \cdot \text{h}^{-1}$.

Table 1

Performances of catalysts with low W surface density.^a

Catalyst ^b	Conversion (%)	Selectivity (%)				
		1,3-PDO	1,2-PDO	1-PO	2-PO	others
Pt/ZrW5(600)	7.1	4.5	71.2	5.7	0.0	18.6
Pt/ZrW5(700)	5.7	8.5	71.4	5.2	0.8	14.1
Pt/ZrW5(800)	6.0	17.6	55.2	13.3	2.8	11.1
Pt/ZrW5(900)	5.7	30.1	42.0	16.1	4.4	7.4
Pt/ZrW10	7.5	29.8	44.9	15.0	3.5	6.8
Pt/ZrW10Mn1	6.0	8.7	73.4	5.4	1.3	11.2

^a Reaction conditions are the same as those in Fig. 3.

^b The calcination temperature of ZrW5 is denoted in bracket.

3.1.3. Performances of catalysts with low W surface density

As elucidated above, glycerol hydrogenolysis is structurally sensitive on WO_x domains, and 1,3-PDO selectivity changes significantly at low W surface density region. Here, the WO_x domain size of catalysts with low W surface density was adjusted to provide further evidence. For supported WO_x materials, WO_x polymerization is also effected by calcination temperature [20,43,45]. As shown in Table 1, with the calcination temperature of ZrW5 raising from 600 °C to 900 °C, 1,3-PDO selectivity is significantly increased from 4.5% to 30.1%, indicating that polymerized WO_x has a great advantage over isolated WO_x in 1,3-PDO formation. For Pt/ZrW10 which has medium polymerized WO_x at sub-monolayer, the selectivity of 1,3-PDO is 29.8% (Table 1, entry 5). However, with the addition of 1% Mn element, 1,3-PDO selectivity drops to only 8.7% (entry 6), which is ascribed to the depolymerization of medium sized WO_x by Mn doping.

3.2. Acid properties and nature of the active site

3.2.1. Acid characterization of supports

$\text{NH}_3\text{-TPD}$ profiles of supports are presented in Fig. S3. Generally, weak, medium, and strong acid sites give NH_3 desorption signals at < 200 , 200–350, and 350–450 °C, respectively [51]. ZrO_2 has only a small amount of weak acids as shown in Fig. S3a. With the addition of WO_x , medium and strong acid sites appear and all their amounts are increased, indicating that WO_x domains are the main source of acid sites. Mn doping could consume WO_x species and form nonacid Mn WO_4 particles, thus causing a decrease in the amount of acid (Fig. S3b). For all the oxide supports investigated here, the acid amount follows this trend: weak acid $>$ medium acid $>$ strong acid.

In order to distinguish Brønsted acid and Lewis acid sites, FTIR spectra of pyridine adsorption were also conducted, and quantitative results and the percent of Brønsted acid are given in Fig. 6. For the pure ZrO_2 support, only Lewis acid sites are presented on the surface. When 5% WO_x added, Lewis acid amount is increased by more than 3 times, from 0.008 to 0.027 mmol/g, while only a few Brønsted acid sites are generated (0.006 mmol/g). Further addition of WO_x leads to a mild variation of Lewis acids between 0.027 and 0.035 mmol/g, meanwhile, Brønsted acids are almost linearly increased from 0.006 to 0.052 mmol/g (Fig. 6a). Combined with the structure characterizations of WO_x in Fig. 2, the acid properties presented here indicate that polymerized WO_x domains contribute to the formation of Brønsted acid sites, and Lewis acids are existed on both isolated and polymerized WO_x . When Mn is introduced, Brønsted acids are gradually decreased while the amount of Lewis acid almost remains constant (Fig. 6b). This is related to the consumption of polymerized WO_x , consistent with structure characterizations in Fig. 4.

It should be noted that all the acid properties (acid strength distribution, acid types and amounts) are monotonically changed with the amount of WO_x or Mn. ZrW38 has excellent advantages on acids over other oxide supports, however, the corresponding catalytic performance in glycerol hydrogenolysis is too low. Hence, it is evident that

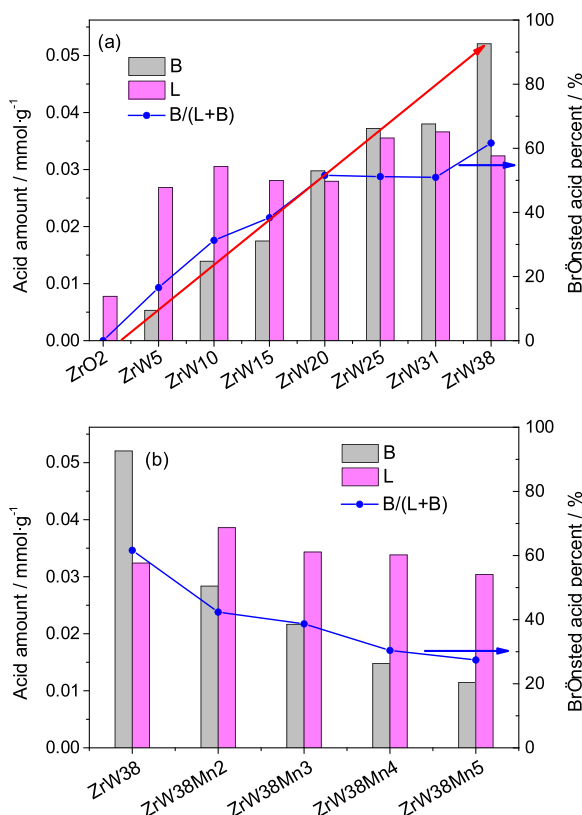


Fig. 6. Brønsted and Lewis acid distributions over (a) ZrWx and (b) ZrW38Mnx. B: Brønsted acid. L: Lewis acid.

there are other factors that impact the reaction.

3.2.2. The interaction between WO_x and Pt

Metal sites also play an important role in glycerol hydrogenolysis, which could influence the hydrogen activation and spillover steps or even change the reaction routes [52–54]. Pt metal dispersion and H/Pt ratio of catalysts are presented in Table 2. H/Pt values are nearly the same (ranging from 0.92 to 1.17), indicating a similar activated hydrogen and spillover capacity between different catalysts. Pt/ZrO₂ has the highest metal dispersion (78.3%) measured by CO chemisorption, but the value drops down to 39.0% with the addition of WO_x (entry 2 and entry 3). For Mn containing samples, the dispersion is scattered in the region 28.6%–39.8%.

In our previous work, TEM and XRD were used to exclude the existence of large Pt particles on Pt/ZrW38, and the low dispersion measured by CO chemisorption was attributed to the partial coverage of Pt surface by WO_x species [53]. Further evidence is given here with DRIFT spectra of CO adsorption (Fig. S4). On Pt/ZrO₂ with high metal dispersion, a strong band of bridging adsorbed CO on Pt surface (1837 cm⁻¹) is presented. Conversely, the band almost disappears on

Table 2
Pt metal dispersion and H/Pt value of different catalysts.

Catalyst	Dispersion ^a (%)	H/Pt ^b
Pt/ZrO ₂	78.3	0.92
Pt/ZrW ₁₅	42.8	1.12
Pt/ZrW ₃₈	39.0	1.16
Pt/ZrW38Mn ₂	35.4	1.17
Pt/ZrW38Mn ₃	28.6	1.14
Pt/ZrW38Mn ₄	30.4	1.04
Pt/ZrW38Mn ₅	39.8	0.99

^a Measured by CO chemisorption at room temperature.

^b Calculated by H₂ chemisorption at 50 °C.

Pt/ZrW38. This is related to the decrease of neighboring Pt atoms on the surface with the partial coverage of WO_x species. With the addition of Mn, WO_x is consumed gradually and the coverage of Pt surface is also weakened, resulted in the observation of bridging adsorption band at 1837 cm⁻¹ again.

The interaction between Pt and WO_x can also be illustrated by Raman spectra in Fig. 7. Compared with Raman results of ZrWx (Fig. 2b) and ZrW38Mnx (Fig. 4b), much difference is shown on the spectra of Pt containing samples. The vibration region of hydrated W=O mode on ZrWx and ZrW38Mnx is shifted from 960 to 990 cm⁻¹ to 900–933 cm⁻¹ after the addition of Pt. Moreover, the W–O–W stretching region at 811–834 cm⁻¹ is much weaker, while the dehydrated W=O mode [46] at 1014 cm⁻¹ is clearly observed on Pt containing samples. Such differences in Raman spectra indicate that the addition of Pt leads to a decrease of connections between WO_x units through W–O–W bond, and an increase of terminal W=O structure, both of which can be ascribed to Pt-WO_x interaction.

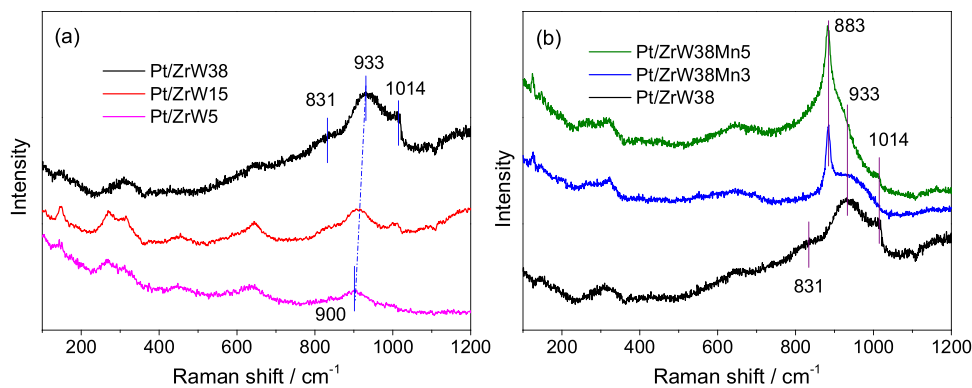
3.2.3. Nature of the active site

Because the structure of WO_x is changed after the addition of Pt metal, it suggests that the acid properties may also be influenced, as the acid sites on the catalysts are almost derived from WO_x domains. NH₃-TPD curves of Pt containing samples are given in Fig. S5. Compared with supports (Fig. S3), NH₃ desorption peak lower than 200 °C is much weaker and the main desorption temperature moves to the region of medium and strong acids. A trailing signal of NH₃ desorption is observed even after 450 °C. This confirms that super strong acid sites are formed after Pt addition, especially on Pt/ZrW38Mn3.

FTIR spectra of pyridine adsorption is not suitable for the acid characterization of Pt containing catalysts in our case, because pyridine is easily reduced to piperidine on the reduced catalysts even after purging under vacuum for 1 h at 350 °C, which causes much difficulty to spectra analysis. To further investigate the strength of Brønsted and Lewis acids, NH₃ adsorbed FTIR combined with temperature programmed desorption process (NH₃-TPD-FTIR) was applied, and the results are presented in Fig. 8. Firstly, FTIR of NH₃ adsorption on Pt/ZrW38Mn3 during TPD was studied and compared with that on ZrW38Mn3. In general, the adsorption band at 1400–1450 cm⁻¹ is assigned to NH₄⁺ bending mode on Brønsted acid sites, and the band at 1220–1240 cm⁻¹ is assigned to the symmetric deformation mode of adsorbed NH₃ on Lewis acid sites [36,55]. With temperature increasing to 450 °C, most of the NH₃ on Lewis acid sites are desorbed while there still remains a lot adsorbed on Brønsted acid sites (Fig. 8a). However, NH₃ is completely desorbed above 400 °C on ZrW38Mn3, as shown in Fig. 8b. This demonstrates that the super strong acids formed by the interaction between WO_x and Pt are Brønsted acid sites. Here this structure is labelled as Pt-(WO_x)_n-H, in which n reflects the polymerization degree of WO_x domains and will be discussed below.

Subsequently, FTIR of NH₃ adsorption on different catalysts at 450 °C was collected and spectra of four typical samples are given in Fig. 8c. The bands of symmetric deformation mode at about 1232 cm⁻¹ almost disappear on all samples, but different intensities of NH₄⁺ bending mode at 1403 cm⁻¹ are observed. So NH₄⁺ band area was calculated and normalized by the weight of catalyst wafer, and its correlation with 1,3-PDO formation rate is given in Fig. 8d. The rate of 1,3-PDO formation is linearly correlated with the band area at 1403 cm⁻¹, confirming that Pt-(WO_x)_n-H with super strong acid is the active site of this reaction.

It should be noted here that only Pt-(WO_x)_n-H with a suitable n value has super strong Brønsted acid property, although the exact range of n is not provided in this study. On the one hand, Pt/ZrW38 with highly polymerized WO_x has little amount of super strong acids and shows poor activity, which can be improved by decreasing WO_x loading or by Mn doping. On the other hand, the performance of Pt/ZrW5 with mainly isolated or low polymerized WO_x can be improved by calcination at higher temperatures (Table 1). Fig. S5 also shows that only

Fig. 7. Raman spectra of (a) Pt/ZrW_x and (b) Pt/ZrW38Mn_x.

medium polymerized WO_x sample (Pt/ZrW38Mn3) has the largest amount of super strong acids with NH₃ desorption peak at > 450 °C.

3.3. Glycerol adsorption, surface hydrogen species, and reaction mechanism

3.3.1. Glycerol adsorption state

The adsorption structure of reactant on the surface is crucial for the reaction route and product selectivity. Up to now, the structure of adsorbed glycerol over WO_x and ReO_x based catalysts has been supposed to be primary alkoxide (or 2,3-dihydroxypropoxide) by most reports, which is thought to have minimal steric repulsion and benefit to 1,3-PDO selectivity [12,13,15,32]. But Feng et al. pointed out that alkoxide is sensitive to water and easy to hydrolyze [30]. Due to the low vapor pressure and the presence of water, experimental studies on glycerol adsorption are challenging and rarely reported. Copeland et al. prepared samples by ex situ wet impregnation of glycerol aqueous solution, and investigated the surface interactions of glycerol with various metal oxides using FTIR spectroscopy [56]. They found glycerol forms multidentate alkoxide surface species with its primary –OH on Lewis acid sites, even in the presence of bulk water. Meanwhile, the secondary –OH only interacts with basic surface oxygen atom through hydrogen

bond. More recently, García-Fernández et al. studied glycerol adsorption states on WO₃/Al₂O₃ and Al₂O₃ surface using ATR-IR spectroscopy. They proposed that primary alkoxide is presented on both WO_x and Al₂O₃ site, while the interaction between glycerol and WO_x surface is stronger [13]. However, they only investigated the conditions on oxide supports and ignored the influence of metal site on WO_x structure and surface properties, which could result in different glycerol adsorption states.

In this part, the adsorption states of glycerol on Pt/ZrO₂ and Pt/ZrW38Mn3 catalysts were studied using FTIR. Similar with the method reported by Copeland et al. [56], the sample wafer was saturated with water and then about 2 μL dilute aqueous solution with glycerol concentration of 1.0 wt.% was used to prepare the adsorbed samples, which could ensure well infrared spectra of chemical adsorbed glycerol. Firstly, the effect of Pt was investigated under room temperature. As shown in Fig. 9a, for pure glycerol, the bands observed at 1108 and 1037 cm⁻¹ are ascribed to 2° and 1° alcohol νCO bands, respectively [13,56]. After adsorption on ZrO₂, the bands are shifted to 1115 and 1062 cm⁻¹, indicating both hydroxyl groups are interacted with ZrO₂ surface. Because the blueshift of 2° νCO is much smaller than that of 1° νCO, it's reasonable to regard the interaction between 2° –OH and ZrO₂

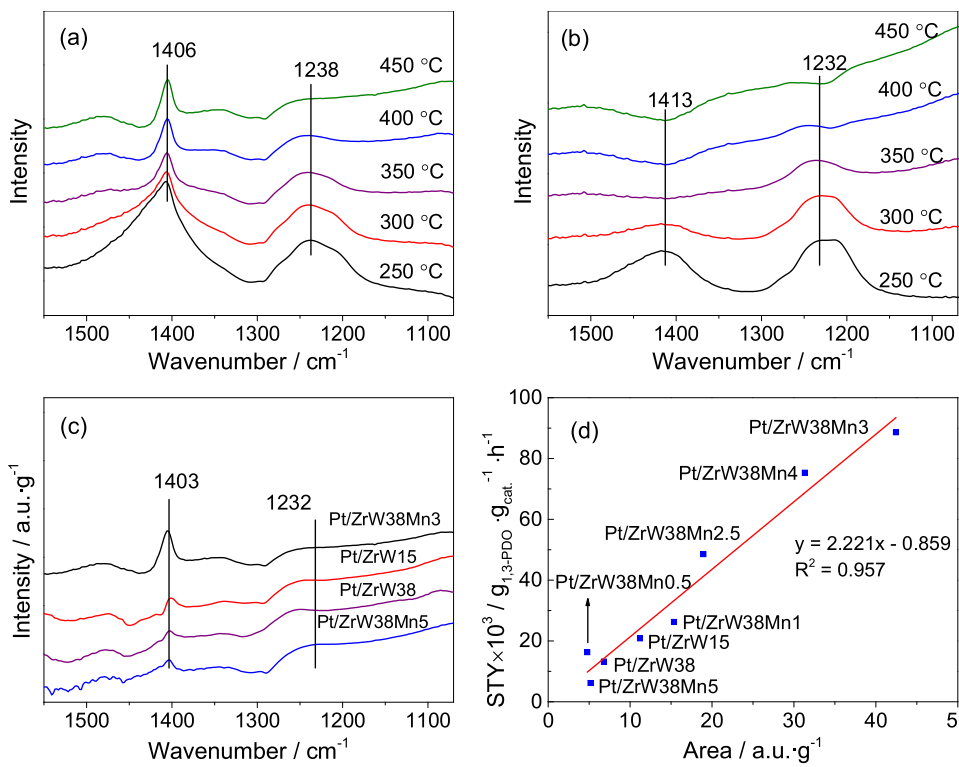


Fig. 8. Acid properties characterization using NH₃ adsorbed FTIR. (a) NH₃-TPD-FTIR of Pt/ZrW38Mn3. (b) NH₃-TPD-FTIR of ZrW38Mn3. (c) NH₃ adsorbed FTIR on four typical catalysts at 450 °C. (d) The correlation between 1,3-PDO formation rate and band area at 1403 cm⁻¹. STY is defined as the amount of 1,3-PDO (g) produced per gram catalyst per hour.

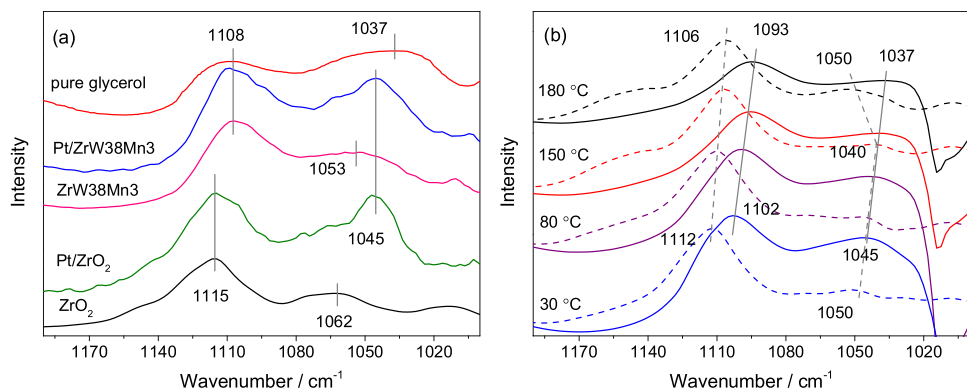


Fig. 9. Adsorption states of glycerol on ZrO₂ and ZrW38Mn3 based samples. (a) Effect of Pt on glycerol adsorption at room temperature with the coexistence of bulk water. (b) Glycerol adsorption states at different temperature under He flow on Pt/ZrO₂ (dotted line) and Pt/ZrW38Mn3 (solid line).

as a weak hydrogen bonding mode with surface base oxygen atom. And correspondingly, the interaction of 1° –OH is assigned to the strong adsorption on surface Lewis acid sites as alkoxide species. This is consistent with the result reported by Copeland et al. [56]. After the introduction of Pt, 2° νCO band is not influenced, but the position of 1° νCO band is shifted from 1062 to 1045 cm⁻¹, much closer to the position for pure glycerol (1037 cm⁻¹). This indicates a weaker adsorption of 1° –OH after the introduction of Pt. As Pt clusters can be anchored to Lewis acid sites [57,58], the weaker adsorption observed here may be considered as weak hydrogen bonding mode between 1° –OH and base oxygen atom on Pt/ZrO₂ surface, similar to the adsorption type of 2° –OH. Also, the adsorption of 1° –OH on weak Lewis acid sites remaining on Pt/ZrO₂ surface can't be excluded. Consistent with that on Pt/ZrO₂, the obvious blueshift of 1° νCO band on ZrW38Mn3 (from 1037 to 1053 cm⁻¹) is also weakened to 1045 cm⁻¹ after the introduction of Pt. However, 2° –OH does not have any interaction with ZrW38Mn3 and Pt/ZrW38Mn3 surface, as the position of 2° νCO band is always stay at 1108 cm⁻¹, same to that of pure glycerol.

The significant blueshift of 1° νCO band on ZrO₂ and ZrW38Mn3 detected in Fig. 9a indicates the strong interaction between 1° –OH and Lewis acid sites, which reflects the existence of primary alkoxide mode on oxide surface. However, Pt particles block these sites and result in a much weaker adsorption of 1° –OH. So the primary alkoxide mode, mentioned in the reaction mechanisms in many reports, is not likely to exist on Pt containing catalysts under room temperature.

The introduction of Pt only changes the adsorption state of 1° –OH but has no effect on 2° –OH, confirming that the adsorption site of 2° –OH is different from that of 1° –OH. In fact, the only difference of glycerol adsorption spectra between Pt/ZrW38Mn3 and Pt/ZrO₂ is that, the 2° –OH group is not interacted with Pt/ZrW38Mn3 but it is weakly bonded to surface oxygen atoms on Pt/ZrO₂. It is still confused that how 2° –OH group is activated without interaction with the catalyst, and further evidence should be provided.

The adsorption states of glycerol on Pt/ZrO₂ and Pt/ZrW38Mn3 at different temperature under He flow are shown in Fig. 9b. As water desorption was ineluctable during temperature increasing, samples were not saturated with water after the reduction. It is clear that water also affects glycerol adsorption states. Compared with moist sample in Fig. 9a, the band of 1° νCO is almost disappeared on Pt/ZrO₂ under He flow at 30 °C, with only a weak signal at 1050 cm⁻¹, while 2° νCO is slightly shifted from 1115 to 1112 cm⁻¹. However, the influence of water is much different on Pt/ZrW38Mn3, the band position of 1° νCO does not change but a clear redshift occurs on 2° νCO, from 1108 (the state of pure glycerol) to 1102 cm⁻¹, indicating a different type of interaction between 2° –OH and this catalyst is presented. Considering that Brønsted acid exists on WO_x based catalyst and plays an important role for the formation of 1,3-PDO, the redshift of 2° νCO band here is assigned to the adsorption of 2° –OH on Brønsted acid site. With

temperature increasing, the degree of blueshift for 2° νCO and 1° νCO are both weakened on Pt/ZrO₂, demonstrating a gradual decrease of the adsorption strength of glycerol. At 180 °C, a blueshift to 1050 cm⁻¹ is observed again for 1° νCO, which may be ascribed to the activation of 1° –OH group or the structure change of glycerol on Pt/ZrO₂ at this temperature. On the surface of Pt/ZrW38Mn3, the blueshift of 1° νCO peak is also weakened (from 1045 to 1037 cm⁻¹) with the increasing temperature. However, the redshift of 2° νCO peak becomes more obvious during the process, from 1102 to 1093 cm⁻¹, which is far from the 2° νCO band of pure glycerol (1108 cm⁻¹). This indicates a stronger interaction between Brønsted acid and 2° –OH on Pt/ZrW38Mn3 at higher temperature, giving a direct evidence of 2° –OH activation on Brønsted acid of the catalysts.

It is hard to observe glycerol adsorption state on catalysts under the real reaction condition (hydrothermal environment at 180 °C) by FTIR method, but the results in Fig. 9 also reflect important information. As elucidated above, the existence of Pt and water can weaken the adsorption of 1° –OH, which suppresses the formation of primary alkoxide species. Water has little effect on the 2° –OH adsorption state on Pt/ZrO₂, but it can weaken the adsorption strength of 2° –OH on Brønsted acid sites of Pt/ZrW38Mn3. At 180 °C, 1° –OH is strongly adsorbed on Pt/ZrO₂ but 2° –OH has almost no interaction with the surface. However on Pt/ZrW38Mn3, the adsorption of 1° –OH is much weaker while 2° –OH is strongly adsorbed on Brønsted acid sites. For a long time, Brønsted acid has been proposed to play an important role in 1,3-PDO formation over Pt-WO_x based catalysts, but the direct evidence of its interaction with glycerol has not been reported until this work. Interestingly, the widely mentioned primary alkoxide species in reaction mechanisms is found to form on Lewis acid sites on the supports (consistent with the comprehensive study from Copeland et al. [56]), but does not seem likely exist on Pt containing catalysts under hydrothermal environment.

3.3.2. Surface hydrogen species

As mentioned in the introduction, five types of surface hydrogen species (Fig. 1) may exist on Pt/WO_x/ZrO₂ based catalysts, and it's still not clear which is participated in glycerol hydrogenolysis to 1,3-PDO. In this part, FTIR spectroscopy is used to give detail information of the existed surface hydrogen species.

Firstly, the Brønsted acid type (permanent or temporary) of active site Pt-(WO_x)_n-H is determined. As temporary Brønsted acid is formed by the partial reduction of WO_x species in hydrogen atmosphere [35,36], it could disappear after exposed to O₂. In order to elucidate it, FTIR of NH₃ adsorption on Pt/ZrW38Mn4 was carried out at 450 °C under O₂. As shown in Fig. S6, the band of NH₄⁺ bending modes at 1403 cm⁻¹ is observed under O₂ atmosphere, with a similar intensity to the result under H₂. This confirms the super strong Brønsted acid of Pt-(WO_x)_n-H is permanent on the surface, but not generated from H₂

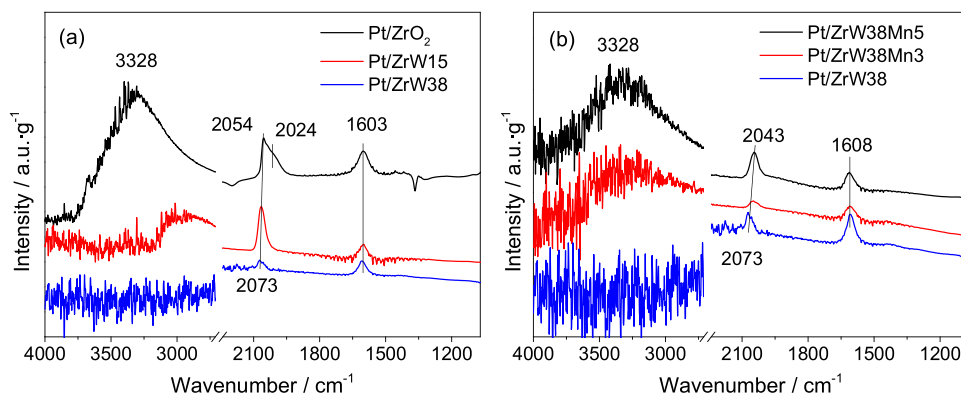


Fig. 10. H_2 adsorbed FTIR on (a) Pt/ZrW_x and (b) Pt/ZrW38Mn_x catalysts.

molecule.

Subsequently, H_2 adsorption FTIR was conducted to identify the types of activated hydrogen species on the catalysts. On Pt/ZrO_2 , two types of hydrogen species are found at 2054 and 2024 cm^{-1} (Fig. 10a), which are assigned to weakly and strongly adsorbed Pt-H , respectively [59]. In addition, strong intensities of H_2O like species derived from hydrogenated ZrO_2 are also presented, with the bending mode at 1603 cm^{-1} and a broad stretching mode at $2500\text{--}3800\text{ cm}^{-1}$ [60]. With the addition of WO_x , the band intensity of Pt-H species is decreased, consistent with the decrease of Pt dispersion (Table 2). In addition, the band position is shifted from 2054 to 2073 cm^{-1} , demonstrating a weaker H_2 adsorption on Pt after the interaction of Pt and WO_x . The H_2O like species are also decreased significantly, which can be related with the coverage of ZrO_2 surface by WO_x . Similar trends are found in H_2 adsorption spectra of Mn containing catalysts (Fig. 10b).

The other types of surface hydrogen species are the hydrides adsorbed on ZrO_2 or WO_x , which are generated from heterolytic dissociation of hydrogen. Generally, Zr-H hydride gives IR band at $1540\text{--}1580\text{ cm}^{-1}$ [37], and W-H hydride at $1980\text{--}1800\text{ cm}^{-1}$ [61]. However, none of these species are observed in Fig. 10. Recently, Copéret et al. reviewed the formation, structure, and reactivity of isolated surface hydrides, and proposed that hydride species adsorbed on WO_3 is unlikely because of the formation of more stable tungsten bronzes [62]. Additionally, Kondo et al. confirmed that Zr-H is observed only after $-\text{OH}$ is removed to some extent at 1003 K [37]. The results in our work are agreed with these studies.

3.3.3. Reaction mechanism

To further elucidate the hydrogenolysis step of secondary $-\text{OH}$, in situ FTIR study of 2-propanol conversion under H_2 was carried out instead of glycerol because of its spectral complexity. Two typical catalysts were chosen in this part, with one of them is good in 1,3-PDO selectivity (Pt/ZrW38Mn3) and the other is poor (Pt/ZrO_2). As presented in Fig. 11, acetone is formed via 2-propanol dehydrogenation on Pt/ZrO_2 , with its characteristic bands at 3090 , 1684 , 1578 and 1095 cm^{-1} [63]. This is accompanied with a strong band emerged at 2006 cm^{-1} , which is assigned to the hydrogen species strongly adsorbed on Pt surface. The δOH band of 2-propanol [63] at 1251 cm^{-1} and water bending mode at 1616 cm^{-1} are not observed on Pt/ZrO_2 . Instead, a broad band assigned to $-\text{OH}$ stretching mode is found at about 3510 cm^{-1} [37,60]. These indicate 2-propanol is dissociated adsorbed on ZrO_2 as alkoxide and surface hydroxyl group, but without further hydrogenolysis to water and propane. Dehydrogenation is the main reaction on Pt/ZrO_2 at $180\text{ }^\circ\text{C}$ even under H_2 (atmospheric pressure), which is consistent with the study on $\text{Pt/Al}_2\text{O}_3$ catalyst [63]. However on Pt/ZrW38Mn3 , none of these species are shown in the spectrum. The characteristic bands of propene at about 3077 , 1645 , and 1444 cm^{-1} are also not presented. Only the consumption of weakly bonded Pt-H (2076 cm^{-1}) and formation of water (1616 cm^{-1}) are

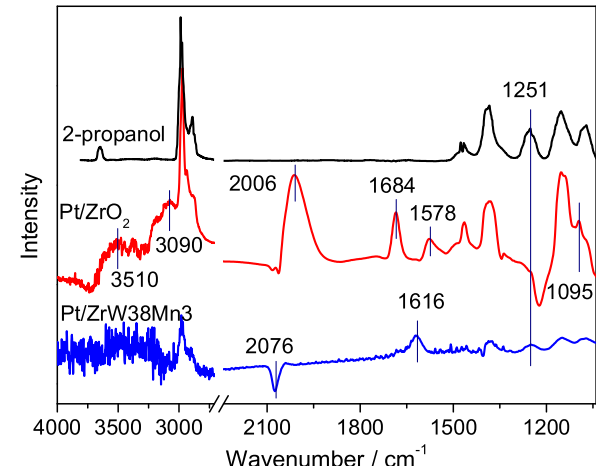


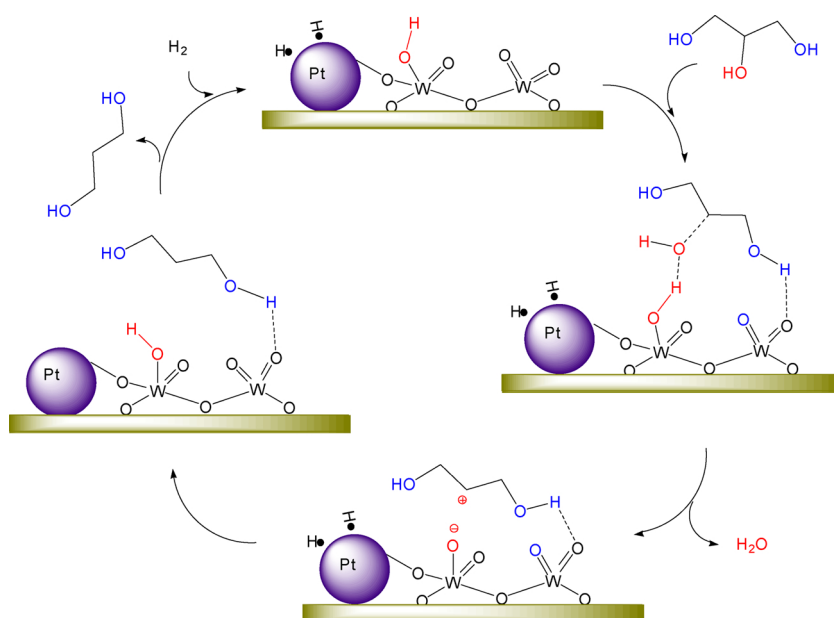
Fig. 11. In situ FTIR study of 2-propanol conversion under H_2 .

observed. Thus, 2-propanol hydrogenolysis to propane and water is catalyzed by Pt/ZrW38Mn3 . The reaction is not likely to undergo a two-step dehydration-hydrogenation mechanism, because $-\text{OH}$ (stretching region at $> 3200\text{ cm}^{-1}$) and the intermediate propene should have been observed in IR spectra during dehydration step.

Thus, direct hydrodeoxygénéation mechanism of $2^\circ-\text{OH}$ is proposed in Scheme 2. Although the existence of primary alkoxide is not supported by our study, weak interaction between $1^\circ-\text{OH}$ and the catalyst surface is not excluded here. The active structure is $\text{Pt-(WO}_x)_n\text{-H}$, which combines metal site and super strong Brønsted acid site together. The $2^\circ-\text{OH}$ group of glycerol is protonated by the super strong Brønsted acid of $\text{Pt-(WO}_x)_n\text{-H}$. Then, the formed water is desorbed from the surface and the corresponding 2° carbonium ion intermediate is stabilized by $\text{Pt-(WO}_x)_n^{\delta-}$ species, as it can delocalize excess charge [19]. Subsequently, the weakly adsorbed hydrogen species on Pt site attack the carbonium intermediate and $(\text{WO}_x)_n^{\delta-}$ quickly via the molecular hydrogen-originated protonic acid site route [64], forming 1,3-PDO species and regenerating super strong Brønsted acid.

4. Conclusion

Two methods were used to adjust the WO_x domain size of $\text{Pt/WO}_x/\text{ZrO}_2$ catalysts and their performances were investigated in glycerol hydrogenolysis. The formation of 1,3-propanediol is structurally sensitive to the polymerization degree of WO_x domains, with medium sized WO_x benefit to 1,3-PDO. Compared with the method of changing WO_x loading, depolymerizing WO_x with the monolayer coverage by appropriate Mn doping can generate a large amount of medium polymerized WO_x , thus enhancing 1,3-PDO formation rate significantly. WO_x structure and acid properties of these catalysts were comprehensively



Scheme 2. Reaction mechanism of glycerol hydrogenolysis to 1,3-PDO on super acidic Pt-(WO_x)_n-H structure.

characterized. Super strong Brønsted acid is found to form when medium polymerized WO_x is interacted with Pt particle, which is proportional to the formation rate of 1,3-PDO. In addition, the 2° – OH group of glycerol is strongly adsorbed to Brønsted acid site at reaction temperature, confirmed by infrared spectroscopy. These results point out that Pt-(WO_x)_n-H is the catalytic active structure, providing super strong Brønsted acid site and metallic Pt site adjacent to each other. The corresponding reaction mechanism is involved with steps of secondary carbonium formation and activated hydrogen attack, which is further evidenced by FTIR studies of H₂ adsorption and in situ 2-propanol reaction.

Competing financial interest

The authors declare no competing financial interest.

Acknowledgment

We gratefully thank the financial support from the National Natural Science Foundation of China (21325626, 21706184, U1510203).

Appendix A. Supplementary data

Supplementary material related to this article can be found, in the online version, at doi:<https://doi.org/10.1016/j.apcatb.2018.10.006>.

References

- D. Sun, Y. Yamada, S. Sato, W. Ueda, Glycerol hydrogenolysis into useful C3 chemicals, *Appl. Catal. B: Environ.* 193 (2016) 75–92.
- R.A. Sheldon, Green and sustainable manufacture of chemicals from biomass: state of the art, *Green Chem.* 16 (2014) 950–963.
- I.C. Freitas, R.L. Manfro, M.M.V.M. Souza, Hydrogenolysis of glycerol to propylene glycol in continuous system without hydrogen addition over Cu-Ni catalysts, *Appl. Catal. B: Environ.* 220 (2018) 31–41.
- C. Garcia-Sancho, J.A. Cecilia, J.M. Merida-Robles, J.S. Gonzalez, R. Moreno-Tost, A. Infantes-Molina, P. Maireles-Torres, Effect of the treatment with H₃PO₄ on the catalytic activity of Nb₂O₅ supported on Zr-doped mesoporous silica catalyst case study: Glycerol dehydration, *Appl. Catal. B: Environ.* 221 (2018) 158–168.
- J. Callison, N.D. Subramanian, S.M. Rogers, A. Chutia, D. Gianolio, C.R.A. Catlow, P.P. Wells, N. Dimitratos, Directed aqueous-phase reforming of glycerol through tailored platinum nanoparticles, *Appl. Catal. B: Environ.* 238 (2018) 618–628.
- M.R. Nimlos, S.J. Blanksby, X.H. Qian, M.E. Himmel, D.K. Johnson, Mechanisms of glycerol dehydration, *J. Phys. Chem. A* 110 (2006) 6145–6156.
- J. ten Dam, U. Hanefeld, Renewable chemicals: dehydroxylation of glycerol and polyols, *ChemSusChem* 4 (2011) 1017–1034.
- D.D. Falcone, J.H. Hack, A.Y. Klyushin, A. Knop-Gericke, R. Schlogl, R.J. Davis, Evidence for the bifunctional nature of Pt-Re catalysts for selective glycerol hydrogenolysis, *ACS Catal.* 5 (2015) 5679–5695.
- M. Chia, Y.J. Pagan-Torres, D. Hibbitts, Q.H. Tan, H.N. Pham, A.K. Datye, M. Neurock, R.J. Davis, J.A. Dumesic, Selective hydrogenolysis of polyols and cyclic ethers over bifunctional surface sites on rhodium-rhenium catalysts, *J. Am. Chem. Soc.* 133 (2011) 12675–12689.
- L.Z. Qin, M.J. Song, C.L. Chen, Aqueous-phase deoxygenation of glycerol to 1,3-propanediol over Pt/WO₃/ZrO₂ catalysts in a fixed-bed reactor, *Green Chem.* 12 (2010) 1466–1472.
- S. Garcia-Fernandez, I. Gandarias, J. Requies, M.B. Guemez, S. Bennici, A. Auroux, P.L. Arias, New approaches to the Pt/WO_x/Al₂O₃ catalytic system behavior for the selective glycerol hydrogenolysis to 1,3-propanediol, *J. Catal.* 323 (2015) 65–75.
- J. Wang, X.C. Zhao, N. Lei, L. Li, L.L. Zhang, S.T. Xu, S. Miao, X.L. Pan, A.Q. Wang, T. Zhang, Hydrogenolysis of glycerol to 1,3-propanediol under low hydrogen pressure over WO_x-supported single/pseudo-single atom Pt catalyst, *ChemSusChem* 9 (2016) 784–790.
- S. Garcia-Fernandez, I. Gandarias, J. Requies, F. Soulímani, P.L. Arias, B.M. Weckhuysen, The role of tungsten oxide in the selective hydrogenolysis of glycerol to 1,3-propanediol over Pt/WO_x/Al₂O₃, *Appl. Catal. B: Environ.* 204 (2017) 260–272.
- X.C. Zhao, J. Wang, M. Yang, N. Lei, L. Li, B.L. Hou, S. Miao, X.L. Pan, A.Q. Wang, T. Zhang, Selective hydrogenolysis of glycerol to 1,3-propanediol: manipulating the frustrated lewis pairs by introducing gold to Pt/WO_x, *ChemSusChem* 10 (2017) 819–824.
- Y.Q. Fan, S.J. Cheng, H. Wang, D.H. Ye, S.H. Xie, Y. Pei, H.R. Hu, W.M. Hua, Z.H. Li, M.H. Qiao, B.N. Zong, Nanoparticulate Pt on mesoporous SBA-15 doped with extremely low amount of W was a highly selective catalyst for glycerol hydrogenolysis to 1,3-propanediol, *Green Chem.* 19 (2017) 2174–2183.
- S.H. Zhu, X.Q. Gao, Y.L. Zhu, Y.W. Li, Promoting effect of WO_x on selective hydrogenolysis of glycerol to 1,3-propanediol over bifunctional Pt-WO_x/Al₂O₃ catalysts, *J. Mol. Catal. A: Chem.* 398 (2015) 391–398.
- Y.Q. Fan, S.J. Cheng, H. Wang, J. Tian, S.H. Xie, Y. Pei, M.H. Qiao, B.N. Zong, Pt-WO_x on monoclinic or tetrahedral ZrO₂: crystal phase effect of zirconia on glycerol hydrogenolysis to 1,3-propanediol, *Appl. Catal. B: Environ.* 217 (2017) 331–341.
- M. Hino, K. Arata, Synthesis of solid superacid of tungsten-oxide supported on zirconia and its catalytic action for reactions of butane and pentane, *J. Chem. Soc. Chem. Commun.* (1988) 1259–1260.
- D.G. Barton, S.L. Soled, G.D. Meitzner, G.A. Fuentes, E. Iglesia, Structural and catalytic characterization of solid acids based on zirconia modified by tungsten oxide, *Catal.* 181 (1999) 57–72.
- N. Soutanidis, W. Zhou, A.C. Psarris, A.J. Gonzalez, E.F. Iliopoulos, C.J. Kiely, I.E. Wachs, M.S. Wong, Relating n-pentane isomerization activity to the tungsten surface density of WO_x/ZrO₂, *J. Am. Chem. Soc.* 132 (2010) 13462–13471.
- F.J.P. Schott, P. Balle, J. Adler, S. Kureti, Reduction of NO_x by H₂ on Pt/WO₃/ZrO₂ catalysts in oxygen-rich exhaust, *Appl. Catal. B: Environ.* 87 (2009) 18–29.
- C. Hahn, M. Endisch, F.J.P. Schott, S. Kureti, Kinetic modelling of the NO_x reduction by H₂ on Pt/WO₃/ZrO₂ catalyst in excess of O₂, *Appl. Catal. B: Environ.* 168 (2015) 429–440.
- C.D. Baertsch, K.T. Komala, Y.H. Chua, E. Iglesia, Genesis of Bronsted acid sites during dehydration of 2-butanol on tungsten oxide catalysts, *J. Catal.* 205 (2002) 44–57.
- V.C. dos Santos, K. Wilson, A.F. Lee, S. Nakagaki, Physicochemical properties of

WO_x/ZrO₂ catalysts for palmitic acid esterification, *Appl. Catal. B: Environ.* 162 (2015) 75–84.

[25] T.Y. Kim, D.S. Park, Y. Choi, J. Baek, J.R. Park, J. Yi, Preparation and characterization of mesoporous Zr-WO_x/SiO₂ catalysts for the esterification of 1-butanol with acetic acid, *J. Mater. Chem.* 22 (2012) 10021–10028.

[26] S.H. Zhu, X.Q. Gao, Y.L. Zhu, J.L. Cui, H.Y. Zheng, Y.W. Li, SiO₂ promoted Pt/WO_x/ZrO₂ catalysts for the selective hydrogenolysis of glycerol to 1,3-propanediol, *Appl. Catal. B: Environ.* 158 (2014) 391–399.

[27] K.S. Song, H.B. Zhang, Y.H. Zhang, Y. Tang, K.J. Tang, Preparation and characterization of WO_x/ZrO₂ nanosized catalysts with high WO_x dispersion threshold and acidity, *J. Catal.* 299 (2013) 119–128.

[28] J.H. Lee, C.H. Shin, Y.W. Suh, Higher Bronsted acidity of WO_x/ZrO₂ catalysts prepared using a high-surface-area zirconium oxyhydroxide, *Mol. Catal.* 438 (2017) 272–279.

[29] W. Zhou, N. Soultanidis, H. Xu, M.S. Wong, M. Neurock, C.J. Kiely, I.E. Wachs, Nature of catalytically active sites in the supported WO₃/ZrO₂ solid acid system: a current perspective, *ACS Catal.* 7 (2017) 2181–2198.

[30] S.H. Feng, B.B. Zhao, L. Liu, J.X. Dong, Platinum supported on WO₃-doped aluminosilicate: a highly efficient catalyst for selective hydrogenolysis of glycerol to 1,3-propanediol, *Ind. Eng. Chem. Res.* 56 (2017) 11065–11074.

[31] S.S. Priya, V.P. Kumar, M.L. Kantam, S.K. Bhargava, A. Srikanth, K.V.R. Chary, High efficiency conversion of glycerol to 1,3-propanediol using a novel platinum-tungsten catalyst supported on SBA-15, *Ind. Eng. Chem. Res.* 54 (2015) 9104–9115.

[32] T. Mizugaki, T. Yamakawa, R. Arundhathi, T. Mitsudome, K. Jitsukawa, K. Kaneda, Selective hydrogenolysis of glycerol to 1,3-propanediol catalyzed by Pt nanoparticles AlO_x/WO₃, *Chem. Lett.* 41 (2012) 1720–1722.

[33] Y. Amada, Y. Shimmi, S. Koso, T. Kubota, Y. Nakagawa, K. Tomishige, Reaction mechanism of the glycerol hydrogenolysis to 1,3-propanediol over Ir-ReO_x/SiO₂ catalyst, *Appl. Catal. B: Environ.* 105 (2011) 117–127.

[34] Y. Shimmi, S. Koso, T. Kubota, Y. Nakagawa, K. Tomishige, Modification of Rh/SiO₂ catalyst for the hydrogenolysis of glycerol in water, *Appl. Catal. B: Environ.* 94 (2010) 318–326.

[35] J. Macht, C.D. Baertsch, M. May-Lozano, S.L. Soled, Y. Wang, E. Iglesia, Support effects on Bronsted acid site densities and alcohol dehydration turnover rates on tungsten oxide domains, *J. Catal.* 227 (2004) 479–491.

[36] C.D. Baertsch, S.L. Soled, E. Iglesia, Isotopic and chemical titration of acid sites in tungsten oxide domains supported on zirconia, *J. Phys. Chem. B* 105 (2001) 1320–1330.

[37] J. Kondo, Y. Sakata, K. Domen, K.-i. Maruya, T. Onishi, Infrared study of hydrogen adsorbed on ZrO₂, *J. Chem. Soc. Faraday Trans.* 86 (1990) 397–401.

[38] W.Z. Li, H. Huang, H.J. Li, W. Zhang, H.C. Liu, Facile synthesis of pure monoclinic and tetragonal zirconia nanoparticles and their phase effects on the behavior of supported molybdena catalysts for methanol-selective oxidation, *Langmuir* 24 (2008) 8358–8366.

[39] S. Lecarpentier, J. van Gestel, K. Thomas, M. Houalla, Study of Ir/WO₃/ZrO₂-SiO₂ ring opening catalysts part I: characterization, *J. Catal.* 245 (2007) 45–54.

[40] C. Thomas, Should W surface density of WO_x-ZrO₂ catalysts be calculated with respect to the specific surface area of the sample or that of ZrO₂ only? *J. Phys. Chem. C* 115 (2011) 2253–2256.

[41] D.G. Barton, M. Shtein, R.D. Wilson, S.L. Soled, E. Iglesia, Structure and electronic properties of solid acids based on tungsten oxide nanostructures, *J. Phys. Chem. B* 103 (1999) 630–640.

[42] C.A. Emeis, Determination of integrated molar extinction coefficients for infrared absorption bands of pyridine adsorbed on solid acid catalysts, *J. Catal.* 141 (1993) 347–354.

[43] E.I. Ross-Medgaarden, W.V. Knowles, T. Kim, M.S. Wong, W. Zhou, C.J. Kiely, I.E. Wachs, New insights into the nature of the acidic catalytic active sites present in ZrO₂-supported tungsten oxide catalysts, *J. Catal.* 256 (2008) 108–125.

[44] M.J. Li, Z.H. Feng, G. Xiong, P.L. Ying, Q. Xin, C. Li, Phase transformation in the surface region of zirconia detected by UV Raman spectroscopy, *J. Phys. Chem. B* 105 (2001) 8107–8111.

[45] M. Scheithauer, R.K. Grasselli, H. Knozinger, Genesis and structure of WO_x/ZrO₂ solid acid catalysts, *Langmuir* 14 (1998) 3019–3029.

[46] E.I. Ross-Medgaarden, I.E. Wachs, Structural determination of bulk and surface tungsten oxides with UV-vis diffuse reflectance spectroscopy and Raman spectroscopy, *J. Phys. Chem. C* 111 (2007) 15089–15099.

[47] A. Martinez, G. Prieto, M.A. Arribas, P. Concepcion, J.F. Sanchez-Royo, Influence of the preparative route on the properties of WO_x-ZrO₂ catalysts: a detailed structural, spectroscopic, and catalytic study, *J. Catal.* 248 (2007) 288–302.

[48] M.M. Ostromecki, L.J. Burcham, I.E. Wachs, N. Ramani, J.G. Ekerdt, The influence of metal oxide additives on the molecular structures of surface tungsten oxide species on alumina: I. Ambient conditions, *J. Mol. Catal. A: Chem.* 132 (1998) 43–57.

[49] P.V. Hanh, L.H. Hoang, P.V. Hai, N.V. Minh, X.B. Chen, I.S. Yang, Crystal quality and optical property of MnWO₄ nanoparticles synthesized by microwave-assisted method, *J. Phys. Chem. Solids* 74 (2013) 426–435.

[50] R. Arundhathi, T. Mizugaki, T. Mitsudome, K. Jitsukawa, K. Kaneda, Highly selective hydrogenolysis of glycerol to 1,3-propanediol over a boehmite-supported platinum/tungsten catalyst, *ChemSusChem* 6 (2013) 1345–1347.

[51] F. Jiang, L. Zeng, S.R. Li, G. Liu, S.P. Wang, J.L. Gong, Propane dehydrogenation over Pt/TiO₂-Al₂O₃ catalysts, *ACS Catal.* 5 (2015) 438–447.

[52] W. Zhou, Y.J. Zhao, Y. Wang, S.P. Wang, X.B. Ma, Glycerol hydrogenolysis to 1,3-propanediol on tungstate/zirconia-supported platinum: hydrogen spillover facilitated by Pt(111) formation, *ChemCatChem* 8 (2016) 3663–3671.

[53] W. Zhou, Y.J. Zhao, S.P. Wang, X.B. Ma, The effect of metal properties on the reaction routes of glycerol hydrogenolysis over platinum and ruthenium catalysts, *Catal. Today* 298 (2017) 2–8.

[54] S. Wang, K.H. Yin, Y.C. Zhang, H.C. Liu, Glycerol hydrogenolysis to propylene glycol and ethylene glycol on zirconia supported noble metal catalysts, *ACS Catal.* 3 (2013) 2112–2121.

[55] A. Zecchina, L. Marchese, S. Bordiga, C. Pazè, E. Gianotti, Vibrational spectroscopy of NH₄⁺ ions in zeolitic materials: an IR study, *J. Phys. Chem. B* 101 (1997) 10128–10135.

[56] J.R. Copeland, I.A. Santillan, S.M. Schimming, J.L. Ewbank, C. Sievers, Surface interactions of glycerol with acidic and basic metal oxides, *J. Phys. Chem. C* 117 (2013) 21413–21425.

[57] Z.C. Zhang, B.C. Beard, Agglomeration of Pt particles in the presence of chlorides, *Appl. Catal. A: Gen.* 188 (1999) 229–240.

[58] C.Z. Li, Z.B. Wang, X.L. Sui, L.M. Zhang, D.M. Gu, Ultrathin graphitic carbon nitride nanosheets and graphene composite material as high-performance PtRu catalyst support for methanol electro-oxidation, *Carbon* 93 (2015) 105–115.

[59] L.T. Dixon, R. Barth, J.W. Gryder, Infrared active species of hydrogen adsorbed by alumina-supported platinum, *J. Catal.* 37 (1975) 368–375.

[60] H. Ishikawa, J.N. Kondo, K. Domen, Hydrogen adsorption on Ru/ZrO₂ studied by FT-IR, *J. Phys. Chem. B* 103 (1999) 3229–3234.

[61] E. Le Roux, M. Taoufik, A. Baudouin, C. Coperet, J. Thivolle-Cazat, J.M. Basset, B.M. Maunder, G.J. Sunley, Silica-alumina-supported, tungsten-based heterogeneous alkane metathesis catalyst: Is it closer to a silica- or an alumina-supported system? *Adv. Synth. Catal.* 349 (2007) 231–237.

[62] C. Coperet, D.P. Estes, K. Larmier, K. Searles, Isolated surface hydrides: formation, structure, and reactivity, *Chem. Rev.* 116 (2016) 8463–8505.

[63] M.I. Zaki, M.A. Hasan, L. Pasupuleti, In situ FTIR spectroscopic study of 2-propanol adsorptive and catalytic interactions on metal-modified aluminas, *Langmuir* 17 (2001) 4025–4034.

[64] H. Hattori, Molecular hydrogen-originated protonic acid site, *Stud. Surf. Sci. Catal.* 138 (2001) 3–12.